J. Plasma Phys. (2020), *vol*. 86, 905860519
Published by Cambridge University Press

doi:10.1017/S0022377820001282

Comparison between mirror Langmuir probe and gas-puff imaging measurements of intermittent fluctuations in the Alcator C-Mod scrape-off layer

R. Kube[1,2,†], **A. Theodorsen**[2], **O. E. Garcia**[2], **D. Brunner**[3,4], **B. LaBombard**[4] **and J. L. Terry**[4]

[1]Princeton Plasma Physics Laboratory, Princeton University, Princeton, NJ 08543-451, USA

[2]Department of Physics and Technology, UiT The Arctic University of Norway, N-9037 Tromsø, Norway

[3]Commonwealth Fusion Systems, Cambridge, MA 02139, USA

[4]MIT Plasma Science and Fusion Center, Cambridge, MA 02139, USA

(Received 10 March 2020; revised 11 September 2020; accepted 16 September 2020)

Statistical properties of the scrape-off layer plasma fluctuations are studied in ohmically heated plasmas in the Alcator C-Mod tokamak. For the first time, plasma fluctuations as well as parameters that describe the fluctuations are compared across measurements from a mirror Langmuir probe (MLP) and from gas-puff imaging (GPI) that sample the same plasma discharge. This comparison is complemented by an analysis of line emission time-series data, synthesized from the MLP electron density and temperature measurements. The fluctuations observed by the MLP and GPI typically display relative fluctuation amplitudes of order unity together with positively skewed and flattened probability density functions. Such data time series are well described by an established stochastic framework that models the data as a superposition of uncorrelated, two-sided exponential pulses. The most important parameter of the process is the intermittency parameter, $\gamma = \tau_d/\tau_w$, where τ_d denotes the duration time of a single pulse and τ_w gives the average waiting time between consecutive pulses. Here we show, using a new deconvolution method, that these parameters can be consistently estimated from different statistics of the data. We also show that the statistical properties of the data sampled by the MLP and GPI diagnostic are very similar. Finally, a synthetic GPI signal using only plasma parameters sampled by the MLP shows qualitatively different fluctuation statistics from the measured GPI signal.

Key words: fusion plasma, plasma diagnostics

1. Introduction

The scrape-off layer (SOL) region of magnetically confined plasmas, as used in experiments on fusion energy, is the interface between the hot fusion plasma and material

† Email address for correspondence: rkube@pppl.gov

walls. It functions to direct hot plasma that is exhausted from the closed flux surface volume onto remote targets. In order to develop predictive modelling capability for the expected particle and heat fluxes on plasma facing components of the machine vessel, it is important to develop appropriate methods to characterize the plasma transport processes in the SOL.

In the outboard SOL, blob-like plasma filaments transport plasma and heat from the confined plasma column radially outward toward the main chamber wall. These filaments are elongated along the magnetic field lines and are spatially localized in the radial–poloidal plane. They typically present order-unity relative fluctuations in the plasma pressure. As they constitute the dominant mode of cross-field transport in the SOL, one needs to understand their collective effect on the time-averaged plasma profiles and on the fluctuation statistics of the SOL plasma in order to develop predictive modelling capabilities for the particle and heat fluxes impinging on the plasma-facing components.

Measuring the SOL plasma pressure at a fixed point in space, the footprint of a traversing plasma filament registers as a single pulse. Neglecting the interaction between filaments, a series of traversing blobs results in a time series that is given by a superposition of pulses. Analysis of single-point time-series data, measured in several tokamaks, reveals that they feature several universal statistical properties. First, histograms of single-point time-series data are well described by a gamma distribution (Graves *et al.* 2005; Horacek *et al.* 2005; Garcia *et al.* 2013*a*,*b*; Garcia, Horacek & Pitts 2015; Kube *et al.* 2016; Theodorsen *et al.* 2016; Garcia *et al.* 2017; Garcia & Theodorsen 2017; Kube *et al.* 2018*a*; Theodorsen *et al.* 2018; Kuang *et al.* 2019). Second, conditionally averaged pulse shapes are well described by a two-sided exponential function (Rudakov *et al.* 2002; Boedo *et al.* 2003; Kirnev *et al.* 2004; Garcia *et al.* 2007; D'Ippolito, Myra & Zweben 2011; Banerjee *et al.* 2012; Garcia *et al.* 2013*a*,*b*; Boedo *et al.* 2014; Carralero *et al.* 2014; Kube *et al.* 2016; Theodorsen *et al.* 2016; Garcia *et al.* 2017; Kube *et al.* 2018*a*). Third, waiting times between consecutive pulses are well described by an exponential distribution. (Adámek *et al.* 2004; Garcia *et al.* 2013*a*,*b*, 2015; Kube *et al.* 2016; Garcia *et al.* 2017; Walkden *et al.* 2017; Kube *et al.* 2018*a*; Theodorsen *et al.* 2018). Fourth, frequency power spectral densities (PSDs) of single-point time-series data have a Lorentzian shape. They are flat for low frequencies and decay as a power law for high frequencies. (Garcia *et al.* 2015, 2016, 2017; Theodorsen *et al.* 2016, 2017*a*, 2018; Garcia & Theodorsen 2017; Kube *et al.* 2018*a*) These statistical properties are robust against changes in plasma parameters and confinement modes.

These universal statistical properties provide a motivation to model the single-point time-series data as a superposition of uncorrelated pulses, arriving according to a Poisson process, using a stochastic model framework. (Garcia 2012; Garcia *et al.* 2016; Militello & Omotani 2016; Theodorsen & Garcia 2016; Theodorsen *et al.* 2017*a*). In this framework, each pulse corresponds to the footprint of a single plasma filament. Using a two-sided exponential pulse shape, the stochastic model predicts the fluctuations to be gamma distributed. The analytical expression for the frequency PSD of this process has a Lorentzian shape (Garcia & Theodorsen 2017; Theodorsen, Garcia & Rypdal 2017*b*). The framework furthermore links the average pulse duration time τ_d and the average waiting time between consecutive pulses $\langle\tau_w\rangle$ to the so-called intermittency parameter $\gamma = \tau_d/\langle\tau_w\rangle$. This intermittency parameter gives the shape parameter of the gamma distribution that describes the histogram of data time series and also determines the lowest-order statistical moments of the data time series (Garcia 2012). Recently, it has been shown that using either γ, or τ_d together with $\langle\tau_w\rangle$, each obtained by a different time series analysis method, allow for a consistent parameterization of single-point time-series data (Theodorsen *et al.* 2018). In order to corroborate the ability of the stochastic model framework to parameterize correctly the relevant dynamics of single-point time-series

data measured in SOL plasmas, and in order to establish the validity of using different diagnostics to provide the relevant fluctuation statistics, it is important to compare parameter estimates obtained using a given method and applied to data sampled by different diagnostics measuring the same plasma discharge.

Langmuir probes and gas-puff imaging (GPI) diagnostics are routinely used to diagnose SOL plasmas. Both diagnostics typically sample the plasma with a few megahertz sampling rate and are therefore suitable to study the relevant transport dynamics. Langmuir probes measure the electric current and voltage on an electrode immersed into the plasma. Plasma parameters, such as the electron density and the plasma potential, are commonly calculated assuming a constant electron temperature, whereas in reality the electron temperature also features intermittent large-amplitude fluctuations, similar to the electron density (LaBombard & Lyons 2007; Kube *et al.* 2018*b*; Kuang *et al.* 2019). The rapid biasing that was recently on a scanning probe on Alcator C-Mod (LaBombard & Lyons 2007; LaBombard *et al.* 2014), the so-called 'mirror' Langmuir probe (MLP), allows measurements of the electron density, electron temperature and the plasma potential on a sub-microsecond time scale. Moreover, GPI diagnostics provide two-dimensional images of emission fluctuations with high time resolution. GPI typically consists of two essential parts. A gas nozzle puffs a contrast gas into the boundary plasma. The puffed gas atoms are excited by local plasma electrons and emit characteristic line radiation modulated by fluctuations in the local electron density and temperature. This emission is sampled by an optical receiver, such as a fast-framing camera or arrays of avalanche photo diodes (APDs) (Terry *et al.* 2001; Cziegler *et al.* 2010; Fuchert *et al.* 2014; Zweben *et al.* 2017). These receivers are commonly arranged in a two-dimensional field of view and encode the plasma fluctuations in a time series of fluctuating emission data. A single channel of the receiver optics is approximated as data from a single spatial point and can be compared with electric probe measurements.

Several comparisons between measurements from GPI and Langmuir probes are found in the literature. Frequency spectra of the SOL plasma in ASDEX (Endler *et al.* 1995) and Alcator C-Mod (Zweben *et al.* 2002; Terry *et al.* 2003) calculated from GPI and Langmuir probe measurements are found to agree qualitatively. In other experiments at Alcator C-Mod, it was shown that the fluctuations of the plasma within the same flux tube, measured at different poloidal positions by GPI and a Langmuir probe, show a cross-correlation coefficient of more than 60 % (Grulke *et al.* 2014). A comprehensive overview of GPI diagnostics and comparison with Langmuir probe measurements is given in Zweben *et al.* (2017).

2. Methods

In this contribution we analyse measurements from the GPI and the MLP diagnostics that were made in three ohmically heated plasma discharges in Alcator C-Mod, confined in a lower single-null diverted magnetic field geometry. The GPI was puffing He and imaging the HeI 587 nm line in these discharges. In addition, we also construct a synthetic signal for the 587 nm emission line using the n_e and T_e time-series data reported by the MLP. All plasma discharges had an on-axis magnetic field strength of $B_T = 5.4\ T$ and a plasma current of $I_p = 0.55$ MA. The MLPs were connected to the four electrodes of a Mach probe head, installed on the horizontal scanning probe (Brunner *et al.* 2017). In the analysed discharges, the scanning probe either performs three scans through the SOL per discharge or dwells approximately at the limiter radius for the entire discharge in order to obtain exceptionally long fluctuation time series data. Table 1 lists the line-averaged core plasma density normalized by the Greenwald density (Greenwald 2002) and the configuration of the horizontal scanning probe for the three analysed discharges. It also

Discharge	$\bar{n}_e/n_G$	$\langle n_e\rangle/(\times 10^{19}\ \mathrm{m}^{-3})$	$\langle T_e\rangle/(\mathrm{eV})$	Probe
1 (1160616009)	0.22	0.19	20	Scan
2 (1160616016)	0.45	0.51	15	Scan
3 (1160616018)	0.45	—	—	Dwell

TABLE 1. List of the line-averaged core plasma density normalized to the Greenwald density, the average electron density and temperature at $\rho \approx 8$ mm, and the operational mode of the horizontal scanning probe.

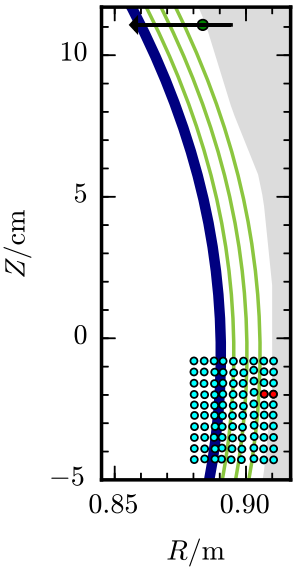

FIGURE 1. A poloidal cross-section of Alcator C-Mod's outboard mid-plane region showing the LCFS (purple line), magnetic flux surfaces in the SOL (green lines), the views of the APDs (cyan dots, red dots show the diode views used in this study), the trajectory of the MLP when scanning (black arrow) and the position where the MLP dwells during discharge 3 (green dot).

lists the average electron density and temperature approximately 8 mm from the last closed flux surface (LCFS), as measured by the MLP and mapped to the outboard mid-plane. These values are representative for the SOL plasma. There is no such data available for discharge 3 because the MLP is dwelled in this case. As discharges 2 and 3 feature almost identical plasma parameters, $\langle n_e\rangle$ and $\langle T_e\rangle$ are likely to be similar in these two discharges.

Figure 1 shows a cut-out of the cross-section of the Alcator C-Mod tokamak. Overlaid are the views of the GPI diodes, the trajectory of the scanning probe head, as well as the position of the LCFS, obtained from magnetic equilibrium reconstruction (Lao *et al.* 1985). The position of the scanning probe in the dwelling position as well as the position of the GPI views used in this study are highlighted.

2.1. *Calculation of synthetic GPI data*

GPI diagnostics are routinely used to measure and visualize fluctuations of the boundary plasma. As realized on Alcator C-Mod, GPI utilizes a vertical stack of four 'barrels', located approximately 1.5 cm beyond the outermost column of views, see figure 1, to puff a contrast gas into the boundary plasma. The line emission arising from the interaction

between the gas atoms and the plasma are captured by a telescope whose optical axis is approximately toroidal and views the puff with sight lines that are approximately normal to the (R, Z)-plane at the toroidal angle of the nozzle. A fiber optic cable carries the light imaged by the telescope to a 9×10 array of APDs which sample it at 2 MHz (Cziegler *et al.* 2010).

The line emission intensity is related to the electron density n_e and temperature T_e as

$$I = n_0 f(n_e, T_e). \tag{2.1}$$

Here, n_0 is the puffed neutral gas density, n_e is the electron density and T_e is the electron temperature. The function f parameterizes the ratio of the density of particles in the upper level of the radiative emission to the ground state density times the rate of decay of the upper level. As discussed in a review by Zweben *et al.* (2017), f is handily parameterized by a power law dependence on the electron density and temperature for perturbations around values of $\langle n_e \rangle$ and $\langle T_e \rangle$ as $f(n_e, T_e) \propto {n_e}^{\alpha} {T_e}^{\beta}$ where exponents α and β are specific to the neutral species used for the diagnostics and are anticipated to depend weakly on n_e and T_e itself. Thus, for small relative fluctuations of n_e and T_e one can assume α and β to be constant. For larger fluctuations, however, one needs to account for variations in the scaling exponents to correctly calculate f. This is further explained in the appendix. Typical values of the fluctuating plasma parameters in the Alcator C-Mod SOL are given by $5 \times 10^{18}\ \mathrm{m}^{-3} \lesssim n_e \lesssim 5 \times 10^{19}\ \mathrm{m}^{-3}$ and $10\ \mathrm{eV} \lesssim T_e \lesssim 100\ \mathrm{eV}$ (LaBombard *et al.* 1997, 2001, 2004; Kube *et al.* 2018*b*, 2019).

For this parameter range the exponents for HeI are within the range $0.2 \lesssim \alpha \lesssim 0.8$ and $-0.4 \lesssim \beta \lesssim 1.0$. Referring to figure 7 in Zweben *et al.* (2017) we note that in this parameter range α decreases monotonously with n_e whereas it varies little with T_e and that β decreases monotonically with T_e whereas it varies little with n_e. Most importantly, f is approximately linear in n_e and T_e for small n_e and T_e whereas f becomes less sensitive to n_e and T_e as they increase.

Equation (2.1) relates the measured line emission intensity to the plasma parameters and is subject to several assumptions. First, the radiative decay rate needs to be faster than characteristic time scales of the plasma fluctuations, neutral particle transport and other atomic physics processes. For the HeI 587 nm line, the radiative decay rate is given by the Einstein coefficient $A \approx 2 \times 10^7\ \mathrm{s}^{-1}$, whereas the turbulence time scale is approximately 10 μs. This shows that atomic processes have equilibrated on the turbulence time scales. Second, n_0 is assumed to be slowly varying in time so that all fluctuations in I can be ascribed to fluctuations in n_e and T_e. This assumption is more questionable and will be discussed further in the next section.

A synthetic line emission intensity signal is constructed using the emission rate f for the 587 nm line of HeI, as calculated by the DEGAS2 code (Stotler & Karney 1994). Interpolating f for the instantaneous n_e and T_e measurements reported by the MLP we calculate

$$I_{\mathrm{syn}} = f(n_e, T_e). \tag{2.2}$$

Note that by using interpolated values of f we avoid using the scaling exponents α and β in the calculation of I_{syn}. Figure 2 illustrates the dependence of I_{syn} on n_e and T_e. Also shown are n_e and T_e values reported by the MLP in the discharges discussed in this paper. This figure is further discussed in § 3. Comparing this expression to (2.1), we note that the puffed-gas density n_0 is assumed to be constant and absorbed into I_{syn}. This method for constructing synthetic GPI emissions is also used by Stotler *et al.* (2003) and Halpern *et al.* (2015). We further note here that a recently developed line-ratio spectroscopy diagnostic that has been implemented at the ASDEX Upgrade tokamak allows n_e and T_e to be

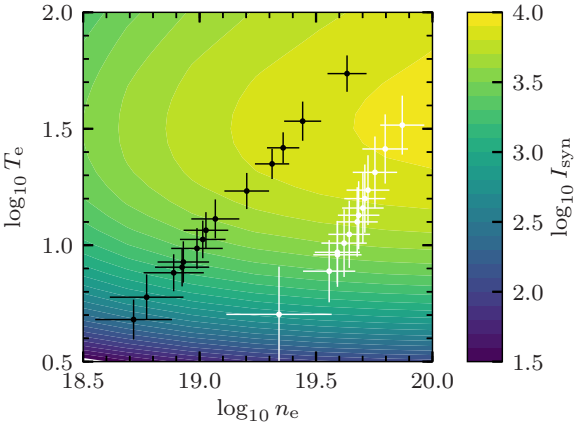

FIGURE 2. Synthetic emission rate for the HeI 587 nm line as a function of the electron density and temperature. Overplotted are the average n_e and T_e values reported by the MLP at different ρ positions in discharge 1 (black markers) and 2 (white markers). The error bars are given by the respective root-mean-square values.

measured directly using information from multiple He line emission in combination with state-of-the-art collisional-radiative models (Muñoz Burgos *et al.* 2012; Griener *et al.* 2017*a*,*b*)

2.2. *Calculation of profiles*

The fluctuations of the plasma parameters can be characterized by their lower order statistical moments, that is, the mean, standard deviation, skewness and excess kurtosis. Scanning the Langmuir probe through the SOL yields a set of I_s, n_e and T_e samples within a given radial interval along the scan path. Here I_s is the ion saturation current. The center of the sampled interval is then mapped to the outboard mid-plane and assigned a ρ_{mid} value, corresponding to the distance from the LCFS. The number of samples within a given interval depends on the velocity with which the probe moves through the SOL as well as the width chosen for the sampling interval. Here, we use only data from the last two probe scans of discharge 1 and 2, as to sample data when the plasma SOL was stable in space and time.

The n_e and T_e data reported by the MLP are partitioned into separate sets for each instance, where the probe is within $\rho_{\mathrm{mid}} \pm \triangle_\rho$, that is, individually for the inward and outward part motion and individually for each probe plunge. Thus, for two probe plunges there are four datasets for n_e and T_e, respectively. The lowest-order statistical moments are calculated from the union of these data sets. To estimate the probability distribution function, the data time series are normalized by subtracting their sample mean and scaling with their respective root-mean-square value. This procedure was chosen to account for variations in the SOL plasma on a time scale comparable with the probe reciprocation time scale and the delay between consecutive probe plunges. Radial profiles of the lowest-order statistical moments of the GPI data can be calculated using the time series of signals from the individual views.

Skewness S and excess kurtosis or flatness, F, of a data sample are invariant under linear transformations. In order to remove low-frequency trends in the data time series, for example, owing to shifts in the position of the LCFS, S and F are calculated after

normalizing the data samples according to

$$\tilde{\Phi} = \frac{\Phi - \langle \Phi \rangle_{\mathrm{mv}}}{\Phi_{\mathrm{rms,mv}}}. \tag{2.3}$$

Here $\langle \Phi \rangle_{\mathrm{mv}}$ denotes a moving average and Φ_{rms} the moving root-mean-square value. Both are calculated using a moving window of approximately 4 ms. This common normalization allows the statistical properties of the fluctuations around the mean to be compared for different data time series using different diagnostic techniques. In the remainder of this article, all data time series are normalized according to (2.3).

2.3. *Parameter estimation*

It has been shown previously that measurement time series of the SOL plasma can be modelled accurately as a superposition of uncorrelated, two-sided exponential pulses. In the following, we discuss how the intermittency parameter γ, the pulse duration time τ_d, the pulse asymmetry parameter λ and the average waiting time between two consecutive pulses $\langle \tau_w \rangle$ are reliably estimated from measurement data.

We obtain the intermittency parameter γ by fitting equation (A9) in Theodorsen *et al.* (2017*b*) on the histogram of the measured time-series data, minimizing the logarithm of the squared residuals.

The PSD for a time series that results from a superposition of uncorrelated exponential pulses is given by (Garcia & Theodorsen 2017)

$$\Omega_{\tilde{\Phi}}(\omega) = \frac{2\tau_d}{[1 + (1-\lambda)^2(\tau_d\omega)^2][1 + \lambda^2(\omega\tau_d)^2]}. \tag{2.4}$$

Here τ_d denotes the pulse duration time and λ denotes the pulse asymmetry. The e-folding time of the pulse rise is then given by $\lambda\tau_d$ and the e-folding time of the pulse decay is given by $(1-\lambda)\tau_d$. We note that the PSD of the entire signal is the same as the PSD of a single pulse. The PSD has a Lorentzian shape, featuring a flat part for low frequencies and a power-law decay for high frequencies. The point of transition between these two regions is parameterized by τ_d and the width of the transition region is given by λ. Note that for very small values of λ the power law scaling can be further divided into a region where the PSD decays quadratically and into a region where the PSD decays as $(\tau_d\omega)^{-4}$ (Garcia & Theodorsen 2017). For the data at hand, PSDs are calculated using Welch's method. This requires long data time series, which excludes data from scanning MLP operation.

Data from the MLP are pre-processed by convolving it with a 12-point boxcar window, that is a rectangular modulation of the signal (LaBombard & Lyons 2007). Assuming that the pulse shapes in the time series of plasma parameters are well described by a two-sided exponential function, the MLP registers such pulses as just this pulse shape filtered with a boxcar window. As the PSD of a superposition of uncorrelated pulses, i.e., the time series of the plasma parameters, is given by the PSD of an individual pulse (Garcia & Theodorsen 2017), the expected power spectrum of MLP data time series is given by the product of (2.4) and the Fourier transformation of a boxcar window:

$$\Omega_{\tilde{\Phi},\mathrm{MLP}}(\omega) = \Omega_{\tilde{\Phi}}(\omega) \times \left[\frac{1}{6\triangle_{\mathrm{t}}\omega}\sin(6\triangle_{\mathrm{t}}\omega)\right]^2. \tag{2.5}$$

Note that this expression holds for raw signals, not for signals normalized according to (2.3). To estimate the duration time τ_d and pulse asymmetry parameter λ, (2.4) is used to fit the GPI data and (2.5) is used to fit the MLP data.

In order to obtain precise waiting time statistics and the a best estimate of τ_w, a method based on Richardson–Lucy (RL) deconvolution is used (Richardson 1972; Lucy 1974). This method was previously used for a comparison of GPI data from several different confinement modes in Alcator C-Mod. The method is described in more detail by Theodorsen *et al.* (2018), here we briefly describe the deconvolution.

By assuming that the dwell MLP and single-diode GPI signals are comprised by a series of uncorrelated pulses with a common pulse shape ϕ and a fixed duration τ_d, the signals can be written as a convolution between the pulse shape and a forcing given by a train of delta pulses,

$$\Phi(t) = [\phi * F]\left(\frac{t}{\tau_d}\right), \tag{2.6}$$

where

$$F(t) = \sum_{k=1}^{K(T)} A_k \delta\left(\frac{t - t_k}{\tau_d}\right). \tag{2.7}$$

The signal Φ can be seen as a train of delta pulses arriving according to a Poisson process F, passed through a filter ϕ. It is therefore called a filtered Poisson process (FPP). For a prescribed pulse shape ϕ and a time series measurement of Φ, the RL deconvolution can be used to estimate F, that is, the pulse amplitudes A_k and arrival times t_k. From the estimated forcing F, the waiting time statistics can be extracted. The RL deconvolution is a point-wise iterative procedure that is known to converge to the least-squares solution (Dell'Acqua *et al.* 2007). For measurements with normally distributed measurement noise, the $n+1$th iteration is given by (Daube-Witherspoon & Muehllehner 1986; Pruksch & Fleischmann 1998; Dell'Acqua *et al.* 2007; Tai, Tan & Brown 2011)

$$F^{(n+1)}(t) = F^{(n)}(t)\frac{[\Phi * \hat{\phi}](t)}{[F^{(n)} * \phi * \hat{\phi}](t)}, \tag{2.8}$$

where $\hat{\phi}(t) = \phi(-t)$. For non-negative Φ and $f^{(0)}$, each following iteration will be non-negative as well. The initial choice $f^{(0)}$ is otherwise unimportant, and has here been set at constant unity. For consistency with PSD estimates of τ_d and λ (see § 3), we use a two-sided exponential pulse function with $\tau_d = 20$ μs and $\lambda = 1/10$ for the GPI data, and a two-sided exponential pulse function with $\tau_d = 10$ μs and $\lambda = 1/25$ convolved with the 12-point window for the MLP data. The deconvolution procedure is robust to small deviations in the pulse shape.

The deconvolution algorithm was run for 10^5 iterations, after which the L^2-norm of the difference between the measured time series and the reconstructed time series was considered sufficiently small. The result of the deconvolution resembles a series of sharply localized, Gaussian pulses, so a peak-finding algorithm is employed in order to extract pulse arrival times and amplitudes from the deconvolved signal. The window size of the peak-finding algorithm is chosen to give the best fit to the expected number of events in the time series, resulting in window sizes of 7.5 μs (I_s), 0.9 μs (n_e), 6.3 μs (T_e), 4.5 μs (GPI, for the view at 90.7 cm) and 7.5 μs (GPI, for the view at 91 cm). The deconvolution procedure finds 85 001, 200 332, 101 815, 30 574 and 17 343 pulses in these time series, respectively.

In order to test the fidelity of the process, a synthetic time series consisting of a pure FPP has been subjected to the deconvolution procedure as well. This time series has the same sampling time, τ_d and λ as the GPI time series, with $\gamma = 2$. In this case, a window

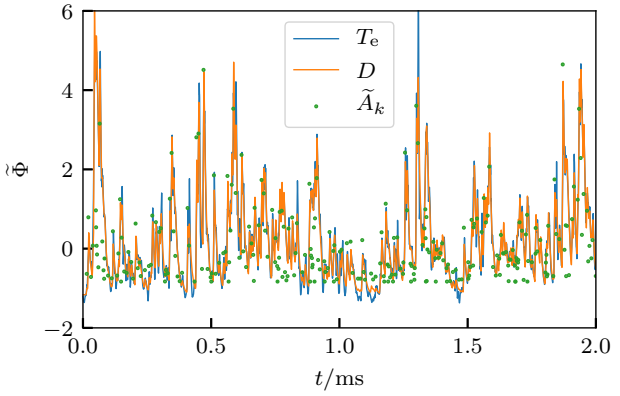

FIGURE 3. Excerpt of original (as measured by the MLP) and reconstructed T_e signals. The blue curve gives the original signal T_e, the green dots indicate arrival times t_k and normalized amplitudes for the pulses A_k and the orange curve gives the reconstructed signal D. All signals are normalized so as to have zero mean and unit standard deviation.

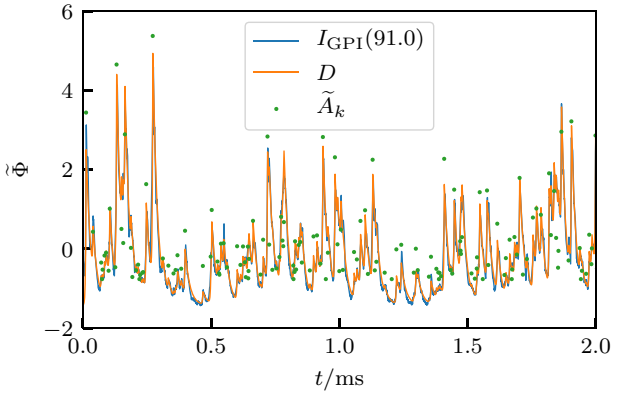

FIGURE 4. Excerpt of original and reconstructed GPI signals at $R = 91$ cm. The blue curve gives the original signal I_{GPI}, the green dots indicate arrival times t_k and normalized amplitudes A_k for the pulses and the orange curve gives the reconstructed signal D. All signals are normalized so as to have zero mean and unit standard deviation.

of 5.5 μs gives the best fit to the expected number of events and the procedure finds 48 011 events (the true number of events in the synthetic time series is 50 000).

Example excerpts of the reconstructed time series are presented in figures 3 and 4. In both figures, the blue lines give the original time series, normalized according to (2.3). The green dots indicate the pulse arrival times and amplitudes that are the output of the deconvolution procedure described previously. The amplitudes have been normalized by their own mean value and standard deviation. By convolving the estimated train of delta pulses with the pulse shape, the full time series is reconstructed. The result of this reconstruction is given by the orange lines. Overall, the reconstruction is excellent. This shows that the deconvolution method can be used to reliably estimate $\langle A \rangle$ and $\langle \tau_w \rangle$ from a given realization of the process or from measurements.

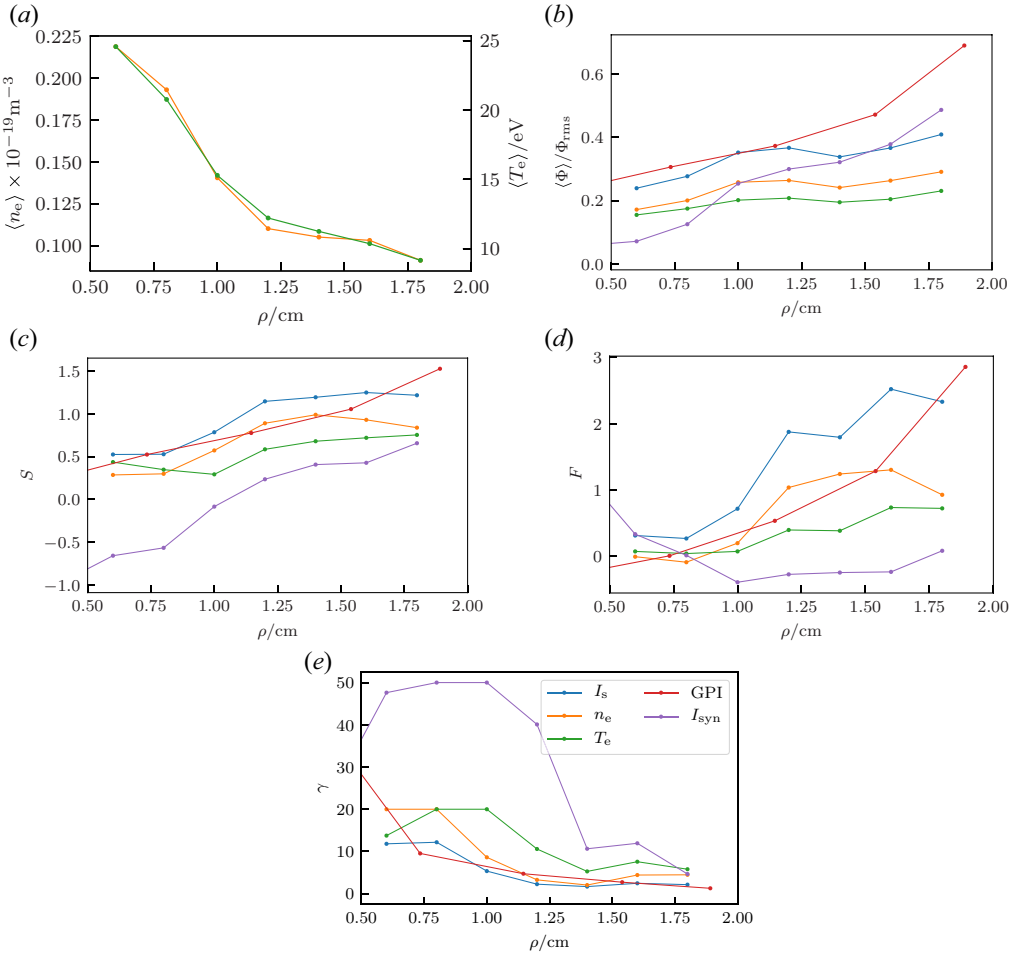

FIGURE 5. Radial profiles of various quantities sampled in discharge 1: (*a*) average; (*b*) relative fluctuation level; (*c*) skewness; (*d*) relative fluctuation level; and (*e*) intermittency parameter. The colour legend in (*e*) applies to all subplots.

3. Results

3.1. *Profiles of MLP, GPI and synthetic GPI data*

Synthetic GPI emission rates are calculated according to (2.2). Discharge 1 features a SOL that is colder and less dense than the SOL plasma in discharge 2. Furthermore, the gradient scale lengths of the $\langle n_e \rangle$ and $\langle T_e \rangle$ profiles are shorter in discharge 1 (Kube *et al.* 2019). Thus, the range of reported n_e and T_e values in discharge 1, shown by black markers in figure 2, is larger than the range reported in discharge 2 (white markers). The contour lines suggest that both $\partial \ln I_{\mathrm{syn}} / \partial \ln T_e$ and $\partial \ln I_{\mathrm{syn}} / \partial \ln n_e$ are larger over the parameter range relevant for discharge 1 than they are for discharge 2. Consequently, variations in the amplitude of the plasma parameters n_e and T_e are mapped in a nonlinear way to variations in the amplitude of I_{syn} and the local fluctuation exponents α and β cannot be used. Appendix A gives a more detailed discussion regarding the local exponent approximation.

We now compare the lowest-order statistical moments of the different signals. Figure 5 shows radial profiles of the mean, the relative fluctuation level, skewness and intermittency

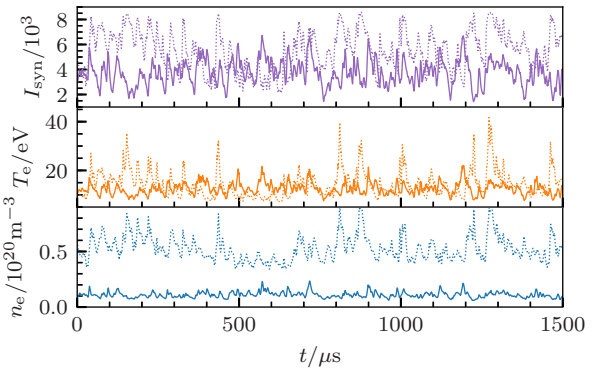

FIGURE 6. Time series of n_e (lowest panel), T_e (middle panel) and synthetic GPI data (top panel) for discharge 1 (full line) and 2 (dashed line). Data are taken in the first interval where the probe scans from $\rho = 1.3$ to 1.2 cm.

parameter for the relevant MLP data (n_e, T_e and I_s), the GPI data, as well as the synthetic GPI data (I_{syn}). Looking at the profile of the average values of n_e and T_e, shown in 5(a) we note that the scale lengths of both quantities are almost identical. Both n_e and T_e decay sharply for $\rho \lesssim 1$ cm. With larger distance from the LCFS their profiles feature a larger scale length. GPI data feature a relative fluctuation level between 0.2 close to the separatrix and larger than 0.6 close to limiter shadow. The MLP data show relative fluctuation levels in the range between approximately 0.2 and 0.4. Both MLP and GPI data feature a fluctuation level of up to 0.5 times their respective mean. This relative fluctuation level increases with distance from the LCFS. The relative fluctuation level of the I_{syn} data also increases with ρ but is less than the fluctuation level of the GPI data (by factors of $\sim$0.85 and $\sim$0.3) over the profile. Coefficients of sample skewness for the MLP and the GPI data are positive, comparable in magnitude and increase with ρ. The synthetic data features negative sample skewness for $\rho \lesssim 1$ cm but are positive and increasing for $\rho \gtrsim 1$ cm. For both MLP and GPI data, F increases from approximately 0 at $\rho \approx 0.5$ cm to larger positive values for $\rho \approx 1.5$ cm. F calculated using I_{syn} data is approximately zero over the entire range of ρ. The lowest panel of figure 5 shows the intermittency parameter γ, obtained by a fit on the histogram of data sampled in a given ρ bin. Both, MLP and GPI data feature a large value of $\gamma \gtrsim 10$ for $\rho \lesssim 1$ cm. This implies that the probability density functions (PDFs) closely follow a normal distribution, which is consistent with small values of S and F. For larger ρ values the data features positively skewed and flattened histograms, a feature captured by the smaller γ value and compatible with the larger estimates of S and F. For the synthetic data, γ is estimated to be larger than 10 over the entire range of ρ. This implies that these samples closely follow a normal distribution, which is compatible with nearly vanishing skewness and excess kurtosis of this data. Although the radial profiles of the lowest-order statistical moments calculated using MLP and GPI data agree qualitatively, the profiles of the I_{syn} data show large discrepancies. The relative fluctuation level of the I_{syn} data is comparable with the relative fluctuation level of the I_s, n_e, T_e and the GPI data, whereas S, F and γ calculated using I_{syn} data correspond to a near-Gaussian process. Figure 6 shows n_e, T_e and I_{syn} time series. The waveforms of the n_e and T_e data present intermittent and asymmetric large-amplitude bursts for both discharge 1 and 2. Peaks in the I_{syn}, on the other hand,appear with a somewhat smaller amplitude relative to the quiet time between bursts and with a more symmetric shape. Histograms of the corresponding data, shown in figure 7, corroborate this interpretation. For the data

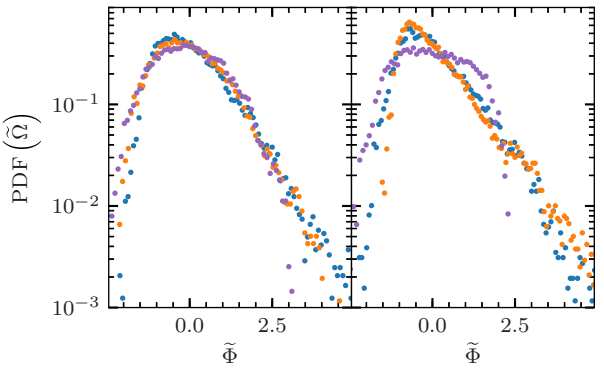

FIGURE 7. Histogram of $\tilde{n}_e$ (blue dots), $\tilde{T}_e$ (orange dots) and $\tilde{I}_{\text{syn}}$ (purple dots) for discharge 1 (left) and 2 (right). Data are taken in all intervals where the probe scans from $\rho = 1.2$ to 1.3 cm.

sampled in discharge 1 (full lines in figure 6 and the left panel in figure 7), histograms of the n_e and T_e data are asymmetric with elevated tails for large-amplitude events. The histogram of the I_{syn} data, on the other hand, features no elevated tail for large-amplitude events. For $\tilde{I}_{\text{syn}} \gtrsim 2.5$ the histogram is approximately zero. For discharge 2 (dashed lines in figure 6 and the right panel in figure 7), the histogram of the I_{syn} data appears symmetric and features a plateau around $\tilde{I}_{\text{syn}} = 0$ without a pronounced peak.

The different fluctuation statistics can be understood by referring to figure 2. For one, I_{syn} is more sensitive to T_e fluctuations than to n_e fluctuations, that is, $\partial I_{\text{syn}}/\partial T_e > \partial I_{\text{syn}}/\partial n_e$ within relevant ranges of n_e and T_e. Fluctuations in n_e and T_e are strongly correlated and feature similar exponential pulse shapes (Kube *et al.* 2018*b*). These are similar to experimentally measured GPI exponential pulse shapes (Garcia 2012; Garcia *et al.* 2013*b*). However, (2.2) will not result in a perfectly scaled pulse shape of the input signals because it depends nonlinearly on both n_e and T_e.

3.2. *Statistical properties of MLP and GPI data*

In the following, we present a statistical analysis of measurements taken from the dwelled MLP in discharge 3. These are compared with GPI data taken from two diode view positions, one radially slightly inside and one slightly outside of the estimated MLP position.

Figure 8 shows the frequency PSDs calculated from MLP and GPI data sampled in discharge 3. The PSDs of the GPI data from the two different radial positions, shown in the left panel, are almost identical. They are flat for low frequencies, $f \lesssim 5$ kHz, before transitioning into a broken power law decay for high frequencies. A least-squares fit of (2.4) on the data (black line) yields $\tau_d \approx 20$ µs and $\lambda \approx 0.1$ and describes the PSDs of the signals perfectly over more than four decades.

PSDs of the MLP data (I_s, n_e, and T_e) appear similar in shape to the PSD of the GPI data, except that for high frequencies, $f \gtrsim 0.2$ MHz, a 'ringing' effect can be observed. This is due to internal data processing of the MLP, which smoothes data with a 12-point uniform filter as discussed previously (Kube *et al.* 2018*b*). Fitting (2.5) on the data yields $\tau_d = 10$ µs and $\lambda = 0.04$. The red and black lines in the right-hand panel show (2.5) and (2.4), respectively, with these parameters. Although (2.5) describes the Lorentzian-like decay of the experimental data as well as the 'ringing' effect at high frequencies,

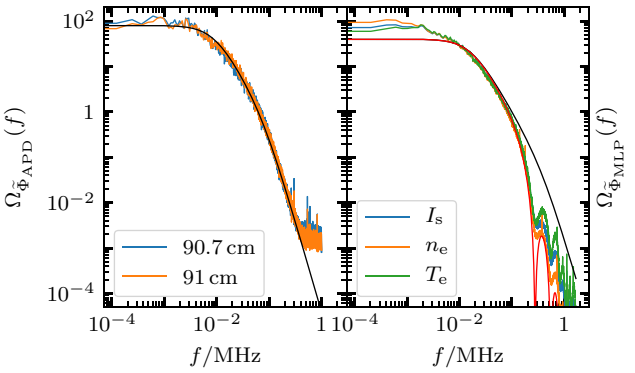

FIGURE 8. Left: PSD of the GPI data from two different radial positions measured in discharge 3 and (2.4) using parameters from a least-squares fit. Right: PSDs of the MLP signals and both (2.5) (red line) and (2.4) (black line) evaluated using parameters found from a least-squares fit.

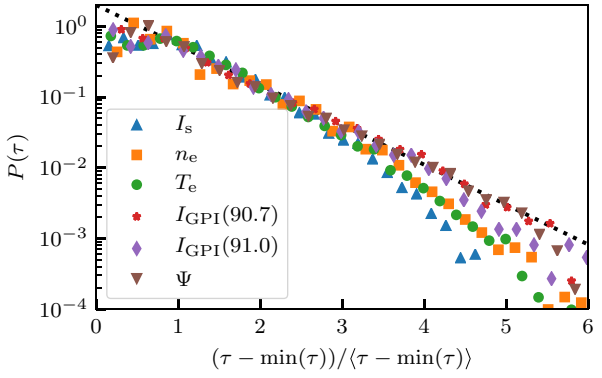

FIGURE 9. PDFs of waiting times obtained from deconvolving the GPI and MLP time series. The synthetically generated time series is indicated by Ψ. The black dotted line indicates exponential decay.

it underestimates the low-frequency part of the spectrum, $f \lesssim 10^{-2}$ MHz. This is addressed by the deconvolution procedure.

Summarizing the parameters found by fitting the GPI and MLP data, we find $\tau_d = 20\,\mu$s and $\lambda = 1/10$ for GPI data and $\tau_d = 10\,\mu$s and $\lambda = 1/25$ for MLP data. In other words, the MLP observes shorter pulses that are more asymmetric than the GPI. As MLP and GPI measure different quantities, such differences might be expected. Other effects, rooted in the specific setup of each diagnostic may also contribute to differences in estimated pulse parameters. GPI measures light emissions from a finite volume (that is at least the 4 mm diameter spot size times the toroidal extent of the gas cloud) and pulses in the signal are due to radially and poloidally propagating blob structures. Therefore, it can be expected that the registered pulses in the signal appear more smeared out compared with those from the Langmuir probes, which measure plasma parameters at the probe tips. Such 'pulse smearing' is less of an issue for the MLP system owing to the small tip size.

Figures 9 and 10 show the results of the deconvolution procedure, starting with the PDF of the waiting times. The brown triangles give the estimated waiting times of the synthetically generated signal, whereas the black dotted line indicates

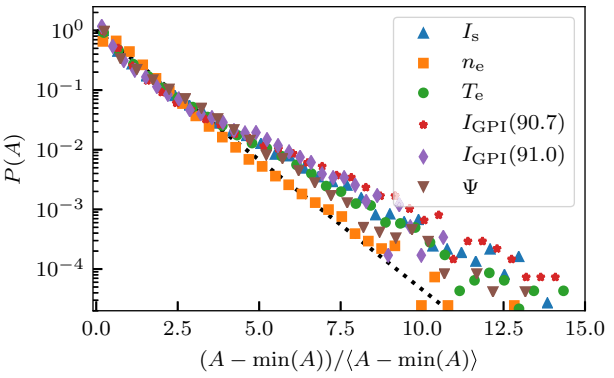

FIGURE 10. PDFs of the pulse amplitudes obtained from deconvolving the GPI and MLP time series. The synthetically generated time series is indicated by Ψ.

an exponential decay. The GPI waiting time distribution conforms very well to the exponential decay of the synthetic time series for the entire distribution. The MLP waiting time distributions decay exponentially over at least two decades in probability. All waiting time distributions have lower probability of small waiting times ($\tau_w/\langle\tau_w\rangle \lesssim 0.8$) compared with an exponential distribution, an artifact of the non-zero τ_d and the peak-finding algorithm. This is also true for the synthetic time series.

Figure 10 shows the PDF of the pulse amplitudes obtained by applying the deconvolution procedure. The pulse amplitudes are approximately exponentially distributed for all analysed signals. The n_e data and the synthetic process Ψ data both appear sub-exponential. On the other hand, the distribution of pulse amplitudes with both GPI data time series appears to be identical to the distribution reconstructed from the I_s and T_e data. For small and large amplitudes, the plotted PDFs show deviations from an exponential function. The deviation for large amplitudes is due to the finite size of the data time series. Deviations for small amplitudes are also observed in other measurement data (Theodorsen *et al.* 2018).

Together, these results indicate that the waiting times derived from the GPI and MLP data follow the same distribution and are consistent with exponentially distributed and independent waiting times. This further justifies using the stochastic model framework. The estimated average waiting times are presented in table 2, and give γ-values consistent with those obtained from fits to the histograms of the time series.

The discrepancy between the low-frequency prediction of (2.4) and the PSD of the MLP data is resolved by the deconvolution procedure. In figure 11, the PSDs of the MLP data time series are presented together with the PSDs of the reconstructed time series and the analytic prediction. Note that the reconstructed time series uses the estimated τ_d and γ as input parameters. We also note that the experimental data has been normalized to their zero moving mean and unity moving root mean square, following (2.3). The length of the used filter is chosen as to remove low-frequency oscillations, but the quality is judged by eye. Thus, the low-frequency part of the spectrum may contain artifacts that are not captured by the stochastic model. The reconstructed time series give the same behaviour for low frequencies as the MLP data, showing that this discrepancy is explainable by the synthetic time series and is not a failure of the model.

Table 2 summarizes the parameter estimation. The first two rows list the parameters estimated using the methods described previously. The parameters listed in the bottom

Parameter	Method	I_s	n_e	T_e	GPI 90 cm	GPI 91 cm
γ	PDF fit	1.01	3.22	1.33	3.54	2.01
$\langle\tau_w\rangle/\mu$s	RL deconv	8.6	3.3	7.1	4.7	9.0
τ_d/μs	PSD fit	9.2	9.7	9.8	19.7	19.1
γ	$\tau_d/\langle\tau_w\rangle$	1.1	2.96	1.39	4.20	2.12

TABLE 2. Process and pulse parameters estimated using MLP and GPI data sampled in discharge 3.

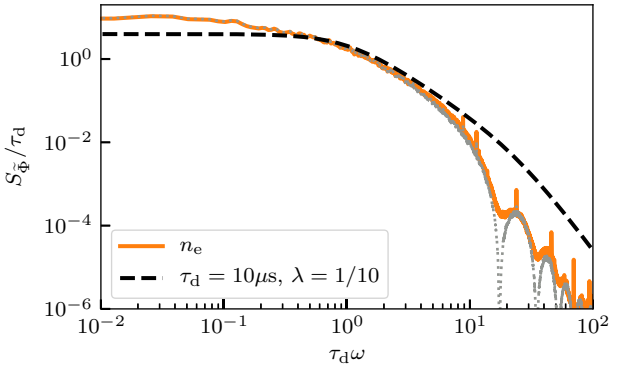

FIGURE 11. Full line: PSDs of MLP time series. Dotted line: Reconstructed time series from the RL deconvolution. The black dashed line gives the PSD predicted by (2.4) for the two-sided exponential pulse.

two rows provide consistency checks for the RL deconvolution. For the I_s and T_e data, we find $\gamma \approx 1$. This describes a strongly intermittent time series with significant quiet time in between pulses. For the n_e time series we find $\gamma \approx 3.2$, comparable with the estimates for the GPI data. The average waiting time between pulses is $\langle\tau_w\rangle \approx 8$ μs. The best estimate for $\langle\tau_w\rangle$ from the n_e time series is given by $\langle\tau_w\rangle \approx 3.3$ μs, estimates from the GPI data are larger by a factor of two or three, depending on the radial position of the view. The pulse duration time for the MLP data is $\tau_d \approx 10$ μs, smaller by a factor of two than for the GPI data, probably for the reasons discussed previously. The difference in average waiting time between n_e and T_e suggests an abundance of blob structures with no or only small temperature variations.

The bottom row lists the intermittency parameter calculated using the estimated pulse duration time and average waiting time, $\gamma = \tau_d/\langle\tau_w\rangle$. The deconvolution algorithm uses τ_d from the power spectrum as an input parameter and γ from the PDF fit as a constraint. Therefore, the fact that $\tau_d/\langle\tau_w\rangle$ is comparable with γ estimated from the PDF fit is a confirming consistency check.

4. Conclusions and summary

Fluctuations of the SOL plasma have been studied for a series of ohmically heated discharges in Alcator C-Mod. It is found that the radial variations of the lowest-order statistical moments, calculated from MLP and GPI measurements, are quantitatively similar. Time-series data from both MLP and GPI diagnostics, feature intermittent, large-amplitude bursts. As shown in numerous previous publications, the time series are

well described as a superposition of uncorrelated pulses with a two-sided exponential pulse shape and a pulse amplitude that closely follows an exponential distribution. In this contribution we demonstrate that the quantities that describe the various parameters of the stochastic process agree across MLP and GPI diagnostics. In particular, the same statistical properties apply to the ion saturation current, electron density and temperature and the line emission intensity.

Radial profiles of the relative fluctuation level, skewness and excess kurtosis, as estimated from both MLP and GPI data, are qualitatively similar and are monotonically increasing with distance from the LCFS. This holds regardless of using I_s, n_e or T_e from the MLP. For the GPI data the time series feature an intermittency parameter $\gamma \approx 2$–3, when estimated from a fit on the PDF. Estimating the intermittency parameter by a fit on the PDF of the different MLP data time series yields $\gamma \approx 3$ for the n_e data and $\gamma \approx 1$ for both the I_s and T_e data. Pulse duration times, estimated from fits on the time series frequency PSD, are $\tau_d \approx 10$ µs for all MLP data time series whereas we find $\tau_d \approx 20$ µs for the GPI data time series. This deviation by a factor of two is likely due to the relatively large in-focus spot size of the individual GPI views. Reconstructing the distributions of waiting times between consecutive pulses from a RL deconvolution, yields average waiting times between pulses of $\langle \tau_w \rangle \approx (3, 7, 9)$ µs for the (n_e, T_e, I_s) data. Using GPI data time series, we find $\langle \tau_w \rangle \approx 5$ and 10 µs for the views at $R = 90.7$ and 91.0 cm, respectively. We note that the GPI view at $R = 91.0$ cm is close to the limiter shadow. Finally, estimating the intermittency parameter as $\tau_d / \langle \tau_w \rangle$ from the deconvolution of the time series gives almost the same values as estimating γ by a fit on the PDF. These findings show that the model parameters of the stochastic model, γ, τ_d and $\langle \tau_w \rangle$, are indeed a good parameterization of the plasma fluctuations, independent of the diagnostic used to measure them. Reconstructing the arrival times and amplitude of the individual pulses using RL deconvolution is an invaluable tool for obtaining the distribution of waiting times between consecutive pulses.

Our analysis also suggests that calculating a synthetic line emission signal using the instantaneous plasma parameters reported by the MLP results in a signal with different fluctuation statistics than the time series actually measured by the GPI. The synthetic time-series data present intermittent pulses, but with a different shape than observed by the GPI. The PDF of these signals furthermore are close to a normal distribution, with low moments of skewness, excess kurtosis and no elevated tails. It is plausible that ionization, where hot plasma filaments locally decrease the puffed gas density, is the main cause of this phenomenon and therefore should be accounted for in such an attempt to reproduce the emission from measurements of n_e and T_e (Thrysøe *et al.* 2016; Wersal & Ricci 2017).

Having established γ, τ_d and $\langle \tau_w \rangle$ as consistent estimators for fluctuations in the SOL, future work will focus on describing their variations with plasma parameters.

Acknowledgements

This work was supported with financial subvention from the Research Council of Norway under Grant No. 240510/F20 and the from the US DoE under Cooperative Agreement No. DE-FC02-99ER54512 40 using the Alcator C-Mod tokamak, a DoE Office of Science user facility. This work was supported by the UiT Aurora Centre Program, UiT The Arctic University of Norway (2020). RK, OEG and AT acknowledge the generous hospitality of the MIT Plasma Science and Fusion Center during a research stay where part of this work was performed. JLT acknowledges the generous hospitality of UiT The Arctic University of Norway and its scientific staff during his stay there.

Editor Troy Carter thanks the referees for their advice in evaluating this article.

Appendix A. Local and global fluctuations

The emission intensity, measured by GPI, is often parameterized as

$$I = n_0 \times f\left(n_e, T_e\right), \tag{A 1}$$

where n_0 is a constant neutral background density. Thus, the differential of I can be written as

$$\frac{\mathrm{d}I}{I} = \frac{\partial \ln f}{\partial \ln n_e}\frac{\mathrm{d}n_e}{n_e} + \frac{\partial \ln f}{\partial \ln T_e}\frac{\mathrm{d}T_e}{T_e}, \tag{A 2}$$

where we use the notation $\partial \ln f(x)/\partial \ln x = (x/f(x))\partial f(x)/\partial x$. Assuming small fluctuation amplitudes, the differential of a function u can be approximated as

$$\frac{\mathrm{d}u}{u} \approx \frac{\triangle u}{u} = \frac{u - \langle u\rangle}{\langle u\rangle + \triangle u} \approx \frac{u - \langle u\rangle}{\langle u\rangle}. \tag{A 3}$$

Here, $\triangle u$ is a small, but non-infinitesimal change in u and $\langle u\rangle$ denotes an average. That is, the relative, infinitesimal change in a function u is approximately the deviation of u to an average $\langle u\rangle$ relative to this average. This approximation gives the local density and temperature exponents α and β:

$$\frac{I - \langle I\rangle}{\langle I\rangle} \approx \alpha\frac{n_e - \langle n_e\rangle}{\langle n_e\rangle} + \beta\frac{T_e - \langle T_e\rangle}{\langle T_e\rangle}, \tag{A 4}$$

where $\alpha = \partial \ln f/\partial \ln n_e$ and $\beta = \partial \ln f/\partial \ln T_e$ at a given (fixed) $\langle n_e\rangle$ and $\langle T_e\rangle$.

For large deviations relative to the mean values, this local approximation breaks down for two reasons. First, the infinitesimal change du can no longer be approximated as a variation relative to a mean value. Second, the partial derivatives in (A 2), which are evaluated at a fixed point, are not necessarily constant when using non-infinitesimal values for dn_e or dT_e. The local exponents are therefore not constant, and the full, global equation (A 1) must be used.

REFERENCES

Adámek, J., Stöckel, J., Hron, M., Ryszawy, J., Tichý, M., Schrittwieser, R., Ionită, C., Balan, P., Martines, E. & Oost, G. V. 2004 A novel approach to direct measurement of the plasma potential. *Czech. J. Phys.* **54** (3), C95.

Banerjee, S., Zushi, H., Nishino, N., Hanada, K., Sharma, S., Honma, H., Tashima, S., Inoue, T., Nakamura, K., Idei, H. *et al.* 2012 Statistical features of coherent structures at increasing magnetic field pitch investigated using fast imaging in Quest. *Nucl. Fusion* **52** (12), 123016.

Boedo, J. A., Myra, J. R., Zweben, S., Maingi, R., Maqueda, R. J., Soukhanovskii, V. A., Ahn, J. W., Canik, J., Crocker, N., D'Ippolito, D. A. *et al.* 2014 Edge transport studies in the edge and scrape-off layer of the national spherical torus experiment with Langmuir probes. *Phys. Plasmas* **21** (4).

Boedo, J. A., Rudakov, D. L., Moyer, R. A., McKee, G. R., Colchin, R. J., Schaffer, M. J., Stangeby, P. G., West, W. P., Allen, S. L., Evans, T. E. *et al.* 2003 Transport by intermittency in the boundary of the DIII-D tokamak. *Phys. Plasmas* **10** (5), 1670–1677.

Brunner, D., Kuang, A. Q., LaBombard, B. & Burke, W. 2017 Linear servomotor probe drive system with real-time self-adaptive position control for the Alcator C-Mod tokamak. *Rev. Sci. Instrum.* **88** (7), 073501.

Carralero, D., Birkenmeier, G., Müller, H., Manz, P., deMarne, P., Müller, S., Reimold, F., Stroth, U., Wischmeier, M., Wolfrum, E. *et al.* 2014 An experimental

investigation of the high density transition of the scrape-off layer transport in ASDEX Upgrade. *Nucl. Fusion* **54** (12), 123005.

CZIEGLER, I., TERRY, J. L., HUGHES, J. W. & LABOMBARD, B. 2010 Experimental studies of edge turbulence and confinement in Alcator C-Mod. *Phys. Plasmas* **17** (5), 056120.

DAUBE-WITHERSPOON, M. E. & MUEHLLEHNER, G. 1986 An iterative image space reconstruction algorthm suitable for volume ECT. *IEEE Trans. Med. Imaging* **5** (2), 61–66.

DELL'ACQUA, F., RIZZO, G., SCIFO, P., CLARKE, R. A., SCOTTI, G. & FAZIO, F. 2007 A model-based deconvolution approach to solve fiber crossing in diffusion-weighted MR imaging. *IEEE Trans. Biomed. Engng* **54** (3), 462–472.

D'IPPOLITO, D. A., MYRA, J. R. & ZWEBEN, S. J. 2011 Convective transport by intermittent blob-filaments: comparison of theory and experiment. *Phys. Plasmas* **18** (6), 060501.

ENDLER, M., NIEDERMEYER, H., GIANNONE, L., KOLZHAUER, E., RUDYJ, A., THEIMER, G. & TSOIS, N. 1995 Measurements and modelling of electrostatic fluctuations in the scrape-off layer of ASDEX. *Nucl. Fusion* **35** (11), 1307.

FUCHERT, G., BIRKENMEIER, G., CARRALERO, D., LUNT, T., MANZ, P., MÜLLER, H. W., NOLD, B., RAMISCH, M., ROHDE, V. & STROTH, U. 2014 Blob properties in L- and H-mode from gas-puff imaging in ASDEX upgrade. *Plasma Phys. Control. Fusion* **56** (12), 125001.

GARCIA, O., KUBE, R., THEODORSEN, A., BAK, J.-G., HONG, S.-H., KIM, H.-S., THE KSTAR PROJECT TEAM & PITTS, R. 2017 SOL width and intermittent fluctuations in KSTAR. *Nucl. Mater. Energy* **12**, 36–43.

GARCIA, O. E. 2012 Stochastic modeling of intermittent scrape-off layer plasma fluctuations. *Phys. Rev. Lett*. **108**, 265001.

GARCIA, O. E., CZIEGLER, I., KUBE, R., LABOMBARD, B. & TERRY, J. L. 2013*a* Burst statistics in Alcator C-Mod SOL turbulence. *J. Nucl. Mater*. **438**, S180–S183.

GARCIA, O. E., FRITZNER, S. M., KUBE, R., CZIEGLER, I., LABOMBARD, B. & TERRY, J. L. 2013*b* Intermittent fluctuations in the Alcator C-Mod scrape-off layer. *Phys. Plasmas* **20**, 055901.

GARCIA, O. E., HORACEK, J. & PITTS, R. A. 2015 Intermittent fluctuations in the TCV scrape-off layer. *Nucl. Fusion* **55** (6), 062002.

GARCIA, O. E., HORACEK, J., PITTS, R. A., NIELSEN, A. H., FUNDAMENSKI, W., NAULIN, V. & RASMUSSEN, J. J. 2007 Fluctuations and transport in the TCV scrape-off layer. *Nucl. Fusion* **47** (7), 667.

GARCIA, O. E., KUBE, R., THEODORSEN, A. & PÉCSELI, H. L. 2016 Stochastic modelling of intermittent fluctuations in the scrape-off layer: correlations, distributions, level crossings, and moment estimation. *Phys. Plasmas* **23** (5), 052308.

GARCIA, O. E. & THEODORSEN, A. 2017 Auto-correlation function and frequency spectrum due to a super-position of uncorrelated exponential pulses. *Phys. Plasmas* **24** (3), 032309.

GRAVES, J. P., HORACEK, J., PITTS, R. A. & HOPCRAFT, K. I. 2005 Self-similar density turbulence in the TCV tokamak scrape-off layer. *Plasma Phys. Control. Fusion* **47** (3), L1.

GREENWALD, M. 2002 Density limits in toroidal plasmas. *Plasma Phys. Control. Fusion* **44** (8), R27.

GRIENER, M., BURGOS, J. M. M., CAVEDON, M., BIRKENMEIER, G., DUX, R., KURZAN, B., SCHMITZ, O., SIEGLIN, B., STROTH, U., VIEZZER, V. *et al.* 2017*a* Qualification and implementation of line ratio spectroscopy on helium as plasma edge diagnostic at ASDEX upgrade. *Plasma Phys. Control. Fusion* **60** (2), 025008.

GRIENER, M., SCHMITZ, O., BALD, K., BÖSSER, D., CAVEDON, M., DE MARNÉ, P., EICH, T., FUCHERT, G., HERRMANN, A., KAPPATOU, A. *et al.* 2017*b* Fast piezoelectric valve offering controlled gas injection in magnetically confined fusion plasmas for diagnostic and fuelling purposes. *Rev. Sci. Instrum*. **88** (3), 033509.

GRULKE, O., TERRY, J. L., CZIEGLER, I., LABOMBARD, B. & GARCIA, O. E. 2014 Experimental investigation of the parallel structure of fluctuations in the scrape-off layer of Alcator C-Mod. *Nucl. Fusion* **54** (4), 043012.

HALPERN, F. D., TERRY, J. L., ZWEBEN, S. J., LABOMBARD, B., PODESTA, M. & RICCI, P. 2015 Comparison of 3d flux-driven scrape-off layer turbulence simulations with gas-puff imaging of Alcator C-Mod inner-wall limited discharges. *Plasma Phys. Control. Fusion* **57** (5), 054005.

HORACEK, J., PITTS, R.A. & GRAVES, J.P. 2005 Overview of edge electrostatic turbulence experiments on TCV. *Czech. J. Phys*. **55** (3), 271–283.

KIRNEV, G. S., BUDAEV, V. P., GRASHIN, S. A., GERASIMOV, E. V. & KHIMCHENKO, L. N. 2004 Intermittent transport in the plasma periphery of the T-10 tokamak. *Plasma Phys. Control. Fusion* **46** (4), 621.

KUANG, A. Q., LABOMBARD, B., BRUNNER, D., GARCIA, O. E., KUBE, R. & THEODORSEN, A. 2019 Plasma fluctuations in the scrape-off layer and at the divertor target in Alcator C-Mod and their relationship to divertor collisionality and density shoulder formation. *Nucl. Mater. Energy* **19**, 295–299.

KUBE, R., GARCIA, O. E., THEODORSEN, A., BRUNNER, D., KUANG, A. Q., LABOMBARD, B. & TERRY, J. L. 2018*a* Intermittent electron density and temperature fluctuations and associated fluxes in the Alcator C-Mod scrape-off layer. *Plasma Phys. Control. Fusion* **60** (6), 065002.

KUBE, R., GARCIA, O. E., THEODORSEN, A., BRUNNER, D., KUANG, A. Q., LABOMBARD, B. & TERRY, J. L. 2018*b* Intermittent electron density and temperature fluctuations and associated fluxes in the Alcator C-Mod scrape-off layer. *Plasma Phys. Control. Fusion* **60** (6), 065002.

KUBE, R., GARCIA, O. E., THEODORSEN, A., KUANG, A. Q., LABOMBARD, B., TERRY, J. L. & BRUNNER, D. 2019 Statistical properties of the plasma fluctuations and turbulent cross-field fluxes in the outboard mid-plane scrape-off layer of Alcator C-Mod. *Nucl. Mater. Energy* **18**, 193–200.

KUBE, R., THEODORSEN, A., GARCIA, O. E., LABOMBARD, B. & TERRY, J. L. 2016 Fluctuation statistics in the scrape-off layer of Alcator C-Mod. *Plasma Phys. Control. Fusion* **58** (5), 054001.

LABOMBARD, B., BOIVIN, R. L., GREENWALD, M., HUGHES, J., LIPSCHULTZ, B., MOSSESSIAN, D., PITCHER, C. S., TERRY, J. L., ZWEBEN, S. J., THE ALCATOR C-MOD GROUP 2001 Particle transport in the scrape-off layer and its relationship to discharge density limit in Alcator C-Mod. *Phys. Plasmas* **8** (5), 2107–2117.

LABOMBARD, B., GOETZ, J., HUTCHINSON, I., JABLONSKI, D., KESNER, J., KURZ, C., LIPSCHULTZ, B., MCCRACKEN, G., NIEMCZEWSKI, A., TERRY, J. *et al.* 1997 Experimental investigation of transport phenomena in the scrape-off layer and divertor. *J. Nucl. Mater*. **241–243**, 149–166.

LABOMBARD, B., GOLFINOPOULOS, T., TERRY, J. L., BRUNNER, D., DAVIS, E., GREENWALD, M. & HUGHES, J. W. 2014 New insights on boundary plasma turbulence and the quasi-coherent mode in Alcator C-Mod using a Mirror Langmuir Probe. *Phys. Plasmas* **21** (5), 056108.

LABOMBARD, B. & LYONS, L. 2007 Mirror Langmuir probe: a technique for real-time measurement of magnetized plasma conditions using a single Langmuir electrode. *Rev. Sci. Instrum*. **78** (7), 073501.

LABOMBARD, B., RICE, J., HUBBARD, A., HUGHES, J., GREENWALD, M., IRBY, J., LIN, Y., LIPSCHULTZ, B., MARMAR, E., PITCHER, C. *et al.* 2004 Transport-driven scrape-off-layer flows and the boundary conditions imposed at the magnetic separatrix in a tokamak plasma. *Nucl. Fusion* **44** (10), 1047.

LAO, L., JOHN, H. S., STAMBAUGH, R., KELLMAN, A. & PFEIFFER, W. 1985 Reconstruction of current profile parameters and plasma shapes in tokamaks. *Nucl. Fusion* **25** (11), 1611.

LUCY, L. B. 1974 An iterative technique for the rectification of observed distributions. *Astron. J*. **79**, 745.

MILITELLO, F. & OMOTANI, J. 2016 Scrape off layer profiles interpreted with filament dynamics. *Nucl. Fusion* **56** (10), 104004.

MUÑOZ BURGOS, J. M., SCHMITZ, O., LOCH, S. D. & BALLANCE, C. P. 2012 Hybrid time dependent/independent solution for the HeI line ratio temperature and density diagnostic for a thermal helium beam with applications in the scrape-off layer-edge regions in tokamaks. *Phys. Plasmas* **19** (1), 012501.

PRUKSCH, M. & FLEISCHMANN, F. 1998 Positive iterative deconvolution in comparison to Richardson–Lucy like algorithms. In *Astronomical Data Analysis Software and Systems VII* (ed. R. Albrecht, R. N. Hook & H. A. Bushouse), pp. 496–499. Astronomical Society of the Pacific Conference Series.

RICHARDSON, W. H. 1972 Bayesian-based iterative method of image restoration. *J. Opt. Soc. Am*. **62** (1), 55.

RUDAKOV, D. L., BOEDO, J. A., MOYER, R. A., KRASHENINNIKOV, S., LEONARD, A. W., MAHDAVI, M. A., MCKEE, G. R., PORTER, G. D., STANGEBY, P. C., WATKINS, J. G. *et al.* 2002 Fluctuation-driven transport in the DIII-D boundary. *Plasma Phys. Control. Fusion* **44** (6), 717.

STOTLER, D. & KARNEY, C. 1994 Neutral gas transport modeling with Degas 2. *Contrib. Plasma Phys.* **34** (2–3), 392–397.

STOTLER, D. P., LABOMBARD, B., TERRY, J. L. & ZWEBEN, S. J. 2003 Neutral transport simulations of gas puff imaging experiments. *J. Nucl. Mater.* **313–316**, 1066–1070.

TAI, Y.-W., TAN, P. & BROWN, M. S. 2011 Richardson–Lucy deblurring for scenes under a projective motion path. *IEEE Trans. Pattern Anal. Mach. Intell.* **33** (8), 1603–1618.

TERRY, J., MAQUEDA, R., PITCHER, C., ZWEBEN, S., LABOMBARD, B., MARMAR, E., PIGAROV, A. & WURDEN, G. 2001 Visible imaging of turbulence in the SOL of the Alcator C-Mod tokamak. *J. Nucl. Mater.* **290–293**, 757–762.

TERRY, J. L., ZWEBEN, S. J., HALLATSCHEK, K., LABOMBARD, B., MAQUEDA, R. J., BAI, B., BOSWELL, C. J., GREENWALD, M., KOPON, D., NEVINS, W. M. *et al.* 2003 Observations of the turbulence in the scrape-off-layer of Alcator C-Mod and comparisons with simulation. *Phys. Plasmas* **10** (5), 1739–1747.

THEODORSEN, A. & GARCIA, O. E. 2016 Level crossings, excess times, and transient plasma–wall interactions in fusion plasmas. *Phys. Plasmas* **23** (4), 040702.

THEODORSEN, A., GARCIA, O. E., HORACEK, J., KUBE, R. & PITTS, R. A. 2016 Scrape-off layer turbulence in TCV: evidence in support of stochastic modelling. *Plasma Phys. Control. Fusion* **58** (4), 044006.

THEODORSEN, A., GARCIA, O. E., KUBE, R., LABOMBARD, B. & TERRY, J. 2017*a* Relationship between frequency power spectra and intermittent, large-amplitude bursts in the Alcator C-Mod scrape-off layer. *Nucl. Fusion* **57** (11), 114004.

THEODORSEN, A., GARCIA, O. E., KUBE, R., LABOMBARD, B. & TERRY, J. L. 2018 Universality of Poisson-driven plasma fluctuations in the Alcator C-Mod scrape-off layer. *Phys. Plasmas* **25** (12), 122309.

THEODORSEN, A., GARCIA, O. E. & RYPDAL, M. 2017*b* Statistical properties of a filtered Poisson process with additive random noise: distributions, correlations and moment estimation. *Phys. Scripta* **92** (5), 054002.

THRYSØE, A. S., TOPHØJ, L. E. H., NAULIN, V., RASMUSSEN, J. J., MADSEN, J. & NIELSEN, A. H. 2016 The influence of blobs on neutral particles in the scrape-off layer. *Plasma Phys. Control. Fusion* **58** (4), 044010.

WALKDEN, N., WYNN, A., MILITELLO, F., LIPSCHULTZ, B., MATTHEWS, G., GUILLEMAUT, C., HARRISON, J., MOULTON, D. & CONTRIBUTORS, J. 2017 Statistical analysis of the ion flux to the JET outer wall. *Nucl. Fusion* **57** (3), 036016.

WERSAL, C. & RICCI, P. 2017 Impact of neutral density fluctuations on gas puff imaging diagnostics. *Nucl. Fusion* **57** (11), 116018.

ZWEBEN, S. J., STOTLER, D. P., TERRY, J. L., LABOMBARD, B., GREENWALD, M., MUTERSPAUGH, M., PITCHER, C. S., HALLATSCHEK, K., MAQUEDA, R. J., ROGERS, B. *et al.* 2002 Edge turbulence imaging in the Alcator C-Mod tokamak. *Phys. Plasmas* **9** (5), 1981–1989.

ZWEBEN, S. J., TERRY, J. L., STOTLER, D. P. & MAQUEDA, R. J. 2017 Invited review article: gas puff imaging diagnostics of edge plasma turbulence in magnetic fusion devices. *Rev. Sci. Instrum.* **88** (4), 041101.